



A light-management film layer induces dramatically enhanced acetate production in photo-assisted microbial electrosynthesis systems

Weifeng Kong^{a,1}, Liping Huang^{a,*1}, Xie Quan^{a,1}, Gianluca Li Puma^{b,*}

^a Key Laboratory of Industrial Ecology and Environmental Engineering, Ministry of Education (MOE), School of Environmental Science and Technology, Dalian University of Technology, Dalian 116024, China

^b Environmental Nanocatalysis & Photoreaction Engineering, Department of Chemical Engineering, Loughborough University, Loughborough LE11 3TU, United Kingdom



ARTICLE INFO

Keywords:

Microbial electrosynthesis
Photocatalysis
Light-management
Al-doped ZnO
Solar-to-acetate

ABSTRACT

A light-management system consisting of a Al-doped ZnO (AZO) film layer was combined for the first time with different bio-photocathodes (*Serratia marcescens* Q1 electrotroph immobilized on g-C₃N₄, MnFe₂O₄ or MnFe₂O₄/g-C₃N₄) to significantly enhance acetate production from bicarbonate in photo-assisted microbial electrosynthesis systems (MES). The AZO light-management system exhibiting optical properties independent of the light incident angle mitigated the shielding effect of light by electrotrophs, increasing light trapping and decreasing light reflection, ultimately allowing higher rates of photon absorption and redistributions of photons over the photo-active layers. As a result, more reducing equivalents as H₂ produced up to 242% (g-C₃N₄/AZO-filter) and 543% (g-C₃N₄/AZO) increase in acetate production at coulombic efficiencies of 70% (g-C₃N₄/AZO-filter) and 81% (g-C₃N₄/AZO). The record high solar-to-acetate efficiency obtained with the MnFe₂O₄/g-C₃N₄/AZO biocathode was 3.20%. The light-management system proposed in this study opens a new promising way to construct efficient bio-photocathodes for inorganic carbon reduction in photo-assisted MES.

1. Introduction

Photo-assisted microbial electrosynthesis (MES) has been proposed as an innovative process for reducing inorganic carbon to key-block chemicals such as acetate, further contributing to achieve a sustainable circular economy based on carbon neutrality [1–4]. Various MES based on hybridized bio-photoactive cathodes combining photocatalysts with electrotrophs such as *Moorella thermoacetica*-CdS [1], *Sporomusa ovata*-Si nanowires/TiO₂/Ni [3] and *Serratia marcescens*-WO₃-MoO₃/g-C₃N₄ [5], have successfully demonstrated the efficient production of acetate from bicarbonate or CO₂. Most of the existing bio-photocathodes are biomimetic or nature-inspired [2,3] and have been engineered by intimately contacting the microbial electrotroph with the photocatalyst interface. However, in such systems the inorganic photocatalyst immobilized on the electrode cannot efficiently absorb the incident light, due to the shielding effect by the dispersed microbial layer. As a consequence, the production of acetate in photo-assisted MES has been limited in term of solar-to-fuel efficiency [4,6].

Recent studies have shown that effective light management in optoelectronic devices such as photoelectrochemical cells and thin-film

photovoltaic cells is a key aspect for producing high system efficiencies [7–10]. With regards to photocatalytic biocathodes, it is essential that the light management substrates deliver high light transmittance and optimal optical haze, as well as excellent electrical conductivity, to efficiently trap the incident light and consequently transfer the photoinduced charge to the interface [6,8,11]. For this purpose, transparent conductive oxide thin films (such as TiO₂ [12,13], Al-doped ZnO (AZO) [14], In₂O₃ and F-doped SnO₂ [12,13]) have been widely used as transparent electrode materials with light management ability in photoelectrochemical cells and dye sensitized solar cells due to their high optical transparency, excellent electron mobility and appreciable high conductivity [12–14]. Among these transparent conductive materials, TiO₂ and AZO have shown more promising application than In₂O₃ and F-doped SnO₂, due to their higher chemical stability and lower resistivity, whereas the highly tunable optical haze of AZO makes it an attractive light management candidate to supplement the transparent electrode field [12,13]. However, to the best of our knowledge, the application and the evaluation of light management techniques in photo-assisted MES has yet to be reported.

Herein, by taking the AZO film as a light-management example and

* Corresponding authors.

E-mail addresses: lipinghuang@dlut.edu.cn (L. Huang), g.liopuma@lboro.ac.uk (G.L. Puma).

¹ College of Chemistry, Dalian University of Technology, Dalian 116024, China.

graphitic carbon nitride ($\text{g-C}_3\text{N}_4$) [15,16] as the photocatalytically active layer, we investigated the role of light management films in photo-assisted MES to provide a strategy to minimize the light shielding obstruction of the immobilized electrotroph (the nonphotosynthetic *S. marcescens* Q1 [5,16]) towards the photocatalytically active $\text{g-C}_3\text{N}_4$ layer. The high optical transparency and suitable optical haze of the AZO light-management film with optical properties independent from the angle of the incident radiation is expected to enhance the transmission of photons through the biocathode, thus increasing the photon flux reaching the $\text{g-C}_3\text{N}_4$ active layer, hence producing more photoinduced reducing equivalents for inorganic carbon reduction into acetate. The photocatalytic performances of MnFe_2O_4 and $\text{MnFe}_2\text{O}_4/\text{g-C}_3\text{N}_4$ heterojunction biocathodes were also evaluated using the AZO film as an effective light management layer, to demonstrate the general applicability of the light-management film proposed here in MES, providing an ideal strategy for delivering efficient acetate production in photo-assisted MES.

2. Materials and methods

2.1. Preparation of photocathodes

The $\text{g-C}_3\text{N}_4/\text{AZO}$ photocathode was prepared through a conventional sol-gel method [17,18]. Briefly, zinc acetate (99.9%) was firstly added in 100 mL of isopropanol (99.8%) with 0.5 h stirring to obtain a concentration of 0.5 M. An equimolar quantity of ethanalamine as sol stabilizer was then added dropwise until the above solution became transparent. After stirring the mixture for 1 h at 80 °C, $\text{Al}(\text{NO}_3)_3 \cdot 9 \text{H}_2\text{O}$ (99.9%) was further dissolved into the mixture to obtain $\text{Al}/(\text{Zn}+\text{Al}) = 2$ at%. The precursor solution was aged for 36 h and then a specific amount of $\text{g-C}_3\text{N}_4$ was dispersed in above solution with 0.5 h ultrasonication. Next, a glass substrate ($2.0 \times 2.0 \times 0.1$ cm, Guluo Glass Co. Ltd, Henan, China) was first immersed into the mixture, remaining inside for around 1 min and then it was extracted with a constant velocity of 1 cm/s and further dried in an oven at 150 °C for 15 min. The dip-coating and drying process was repeated several times in order to produce a film with considerable thickness. The film was finally annealed at 400 °C for 1 h to produce the $\text{g-C}_3\text{N}_4/\text{AZO}$ photocathode. AZO only and $\text{g-C}_3\text{N}_4$ only photocathodes were also prepared following the above procedure without the addition of $\text{g-C}_3\text{N}_4$ or zinc acetate.

The synthesis of $\text{MnFe}_2\text{O}_4/\text{AZO}$ and $\text{MnFe}_2\text{O}_4/\text{g-C}_3\text{N}_4/\text{AZO}$ photocathodes were based on our previous report [19] with modification and briefly described in Supporting Information (SI).

2.2. Characterizations

The phase identification was studied by X-ray diffraction (XRD) using a powder X-ray diffractometer (XRD-6000, Shimadzu, Japan) with Cu K α radiation. Surface composition of the sample was analyzed by X-ray photoelectron spectrometer (XPS, ESCALAB250, Thermo, USA). UV-vis diffuse reflection (UV-vis DRS) and other optical properties were characterized by a Lambda 750 S UV-vis spectrophotometer (Perkin-Elmer, USA). Photoluminescence (PL) spectra were measured on a fluorescence spectrophotometer (F-4500, Hitachi, Japan). The morphology of the photocathode was examined by a scanning electron microscopy (SEM, Nova NanoSEM 450, FEI company, USA) equipped with an energy dispersive X-ray spectroscopy (EDS). High-sensitivity flow cytometry (Accuri C6 Plus, BD company, USA) was employed to assess the electrotrophic viability. Transient photocurrent response was collected by an electrochemical analyzer with 0.1 M Na_2SO_4 electrolyte under light illuminance. Differential pulse voltammetry (DPV) was recorded on an electrochemical workstation (BioLogic, VSP, France) with a scan rate of 0.1 mV/s. In order to exclude any possible false-positive results due to supporting electrolytes or other electroactive considerations, abiotic controls were specifically performed. Electrochemical impedance spectroscopy (EIS) was conducted at a frequency

range from 0.01 to 100 kHz at -1.1 V vs. SHE with an amplitude of 5 mV, where a Zsimpwin software was employed to acquire the Nyquist plots of the impedance spectra. The selected equivalent circuit (Fig. S1) fitted to the photo-assisted MES, provided sufficient information on the surface and material properties of the electrodes, on the electron transfer mechanisms and on the electrotroph metabolism. Specifically, the ohmic resistance (R_s) includes a series of resistances associated with the ohmic transport in the electrolyte (including but not limited to ionic strength and conductivity), and other contact effects (including but not limited to equilibrium-equivalence), as comprehensively described in several studies [20–22].

Photocurrent, DPV and EIS were using a typical three-electrode cell with a working electrode, a Pt counter electrode, and a saturated calomel reference electrode (SCE, +0.241 V versus standard hydrogen electrode (SHE)) reference electrode.

2.3. Reactor construction, electrotroph inoculation and operation

A typical two-chamber reactor separated by a cation exchange membrane (CMI-7000 Membranes International, Glen Rock, NJ) was constructed with internal volumes equal to 28 mL (26 mL effective working volume) in each chamber. The $\text{g-C}_3\text{N}_4/\text{AZO}$ was used as cathode, while a carbon rod along with pieces of graphite felt (0.5 cm × 0.5 cm × 0.5 cm) served as the anode. A SCE was inserted into the cathode chamber. All potentials were recorded versus SHE unless specified.

The anode chamber was inoculated from a microbial fuel cell running on acetate and fed by a nutrient solution [23], while the cathode chamber was inoculated with non-photosynthetic electrotrophic *S. marcescens* Q1 which could efficiently reduce inorganic carbon to produce acetate as previously reported [5]. The catholyte contained NaHCO_3 (23.8 mM), KH_2PO_4 (0.09 mM), NH_4Cl (2.1 mM), mineral 0.6 mL/L and vitamins 0.6 mL/L with the pH of 5.8, whereas an OD_{600} of 0.05, 0.20, 0.35 or 0.50 was employed to inoculate the cathodic chamber. The solution conductivity was adjusted to 103 mS/cm by KCl to form a halophilic environment which has been proven to favor the bioactivity of the halophilic bacteria *Serratia marcescens* for inorganic carbon reduction [2,5]. The anaerobic catholyte was bubbled with N_2 gas (15 min) in an anaerobic glovebox (YQX-II, Xinmiao, Shanghai) to remove all oxygen before adding to the MES reactor. All reactors were kept at 25 ± 3 °C with cathode potentials of -0.6 V, -0.9 V or -1.1 V vs. SHE to investigate the impact of cathode potential on system performance. A 100 W iodine tungsten lamp (light intensity of 23.3 mW/cm²) was used to provide the full spectrum photon flux (Fig. S2) simulating solar light, while experiments with visible light only (named as $\text{g-C}_3\text{N}_4/\text{AZO}$ -filter or $\text{g-C}_3\text{N}_4$ -filter) were conducted under similar procedures, but using a 400 nm UV-cut filter. The schematic diagram of the photo-assisted MES is shown in Fig. S3. The stability of $\text{g-C}_3\text{N}_4/\text{AZO}$ photocathode was evaluated over 12 days operation, with periodical supply of NaHCO_3 to maintain the initial concentration of inorganic carbon at 23.8 mM. All data were recorded after the first operational cycle and all operations were carried out in triplicate.

2.4. Analytical methods

The acetate produced in the catholyte and the residual hydrogen in the cathodic headspace were measured by a gas chromatograph (GC7900, Tianmei, China). The residual inorganic carbon (DZ/T 0064.49–93) and leached Zn (GB 7472–87) in the catholyte were measured by the national standard method. The coulombic efficiency for acetate production (CE_{acetate}) and the solar-to-acetate efficiency (ξ) were obtained through Eqs. 1–2 [3]:

$$CE_{\text{acetate}} = \frac{8 \times n_a \times F}{\int_0^t Idt} \times 100\% \quad (1)$$

$$\xi = \frac{8 \times E^\circ \times n_a \times F}{E_p \times A \times t} \times 100\% \quad (2)$$

where n_a (mol) is the mole of acetate, F (96485 C/mole electron) is the Faraday constant, I (A) is the current, E° is the thermodynamic reduction potential to acetate, E_p (W/cm^2) is the incident photon irradiance, A (cm^2) is the projected area of the cathode, and t (s) is the operation time.

Differences were analyzed by ANOVA in SPSS 19.0 and a p value < 0.05 was regarded as statistically significant.

3. Results and discussion

3.1. Enhanced photoelectrocatalytic performance by the AZO film

The AZO film exhibited a high transmittance of about 93% (Fig. 1A) and an optical haze over 71% (Fig. 1A) with a low reflectance of less than 5% (Fig. 1B), which translated to enhanced light absorption (Fig. 1C) and decreased light reflection (Fig. 1B) of the active layer. After detaching the AZO film from the glass substrate by a scotch tape [24] the high transparency and haze peculiarities of the AZO film were visualized by the clear image obtained (Fig. S4A) as the film closely attached to the printed picture [6,24]. As the distance between the film and picture increased cloudier images were progressively obtained due to the high haze which scattered the light transmitted through the film (Fig. S4B and C). The high transmission haze of the film was further visualized by

the highly scattered and diffused light observed when a red laser ($\lambda = 630 \text{ nm}$) irradiated the screen after passing through the AZO film (Fig. S4D) [24]. In contrast only a small area was illuminated in the bare glass control (Fig. S4E) due to the extremely low haze of the glass substrate (about 1%) [9,24]. The scattering phenomena observed through the AZO film dispersed the light distribution in the active layer by varying the propagation direction of the transmitted light from perpendicular to oblique [25], resulting in a substantially higher fraction of photons being transferred to the active photocatalytic layer and therefore to an overall higher rate of photon absorption.

The UV-vis DRS spectra (Fig. 1C) showed that AZO only absorbed UV light with an absorption edge of 388 nm, corresponding to a band gap (E_g) of 3.20 eV (Fig. 1C inset) [26], while g-C₃N₄/AZO showed a broaden photoabsorption range from UV to visible light [27], attributed to the visible light absorption edge at 454 nm ($E_g: 2.73 \text{ eV}$) of g-C₃N₄. The positive slopes in the Mott-Schottky curves (Fig. S5) confirmed that both AZO and g-C₃N₄ were n-type semiconductors, and that the conduction band edge potential (E_{CB}) was approximately 0.2 V above the flat band potential (E_{FB}) [28]. The energy levels calculated from the Mott-Schottky curves and the formula ($E_{VB} = E_{CB} + E_g$) [27] were: AZO ($E_{CB}: -0.31 \text{ eV}$; valence band edge potential $E_{VB}: 2.89 \text{ eV}$) and g-C₃N₄ ($E_{CB}: -1.15 \text{ eV}$; $E_{VB}: 1.58 \text{ eV}$). The much higher carrier density of g-C₃N₄/AZO ($1.2 \times 10^{18} \text{ cm}^{-3}$) in comparison with the individual semiconductors (AZO: $4.3 \times 10^{17} \text{ cm}^{-3}$; g-C₃N₄: $2.4 \times 10^{17} \text{ cm}^{-3}$) suggested a higher charge conductivity and a smaller charge transfer

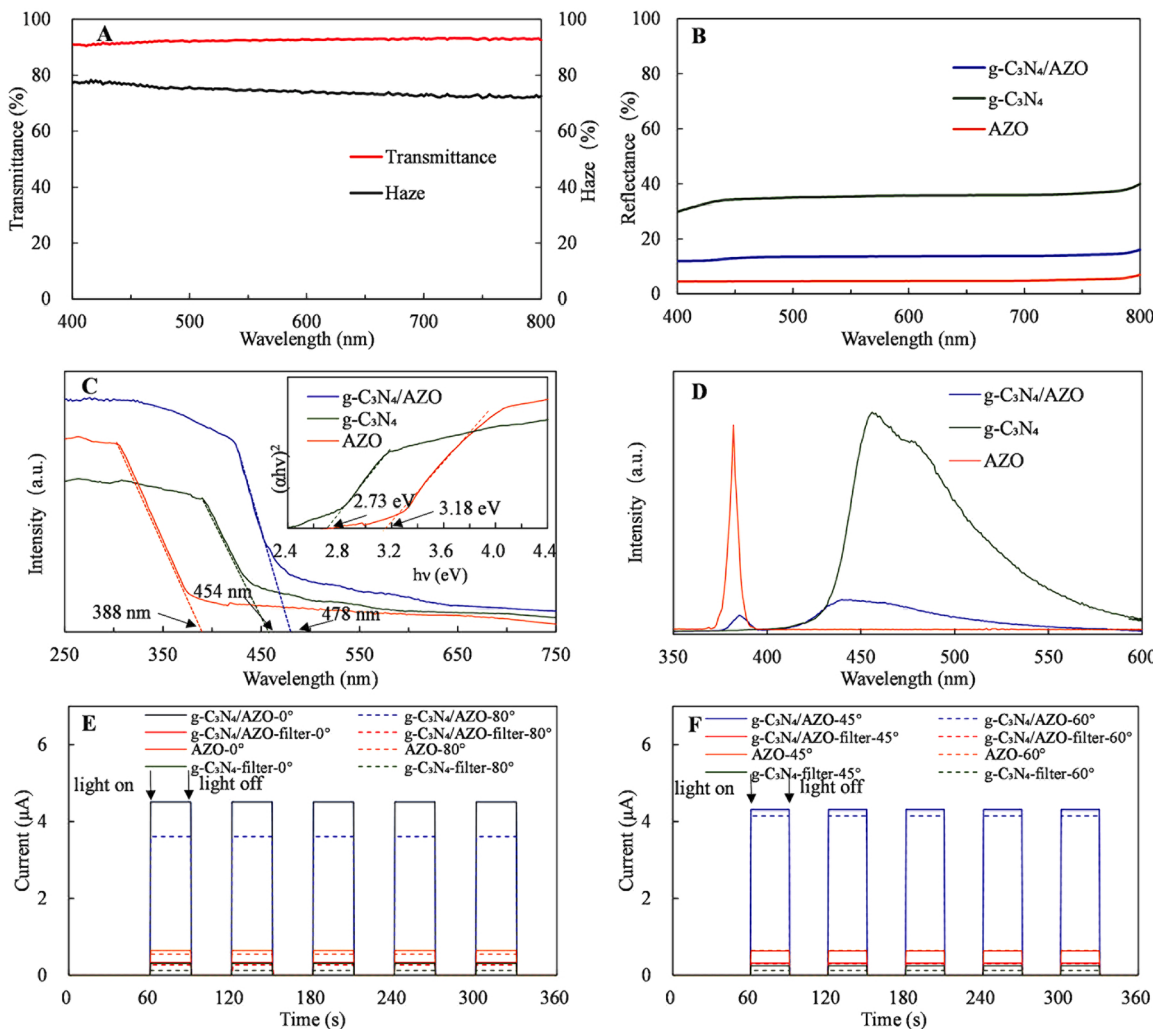


Fig. 1. Light transmittance and haze of the AZO film (A), light reflection (B), UV-vis DRS (C), photoluminescence under 325 nm excitation (D) and transient photocurrent responses with different incident angles (E and F) spectra of various photocatalysts.

resistance in the heterostructure [27,29], which in turn facilitate the photo-assisted reduction of inorganic carbon in this system.

The room temperature PL spectrum of g-C₃N₄/AZO (Fig. 1D) revealed the overlapped emission peaks of AZO (UV emission) and g-C₃N₄ (visible emission) under 325 nm excitation. Although the PL emission of the heterostructure was similar to that of the individual semiconductors, the significant reduction in peak intensity indicated enhanced charge separation in the heterojunction. It is worth noting that g-C₃N₄ had a distinct emission peak, while AZO was not excited under 400 nm excitation (Fig. S6), in agreement with other reports on AZO [11,26]. In other words, AZO cannot be excited under visible light irradiation in the g-C₃N₄/AZO-filter excluding UV light.

Transient photocurrent response tests (Fig. 1E and F) were used to explore the dependence of the optical properties of the AZO film from the angle of the UV-vis incident radiation (shown in Fig. S7), with the incident angle (θ_i) defined as the angle between the incident light and the normal to the receiving surface [9]. The g-C₃N₄/AZO heterostructure obviously exhibited the highest photocurrent and photoinduced carrier efficiency and the lowest recombination efficiency [26,27] when the incident light perpendicularly irradiated the surface of the electrode ($\theta_i = 0^\circ$). The photocurrent of AZO remained almost constant as up to $\theta_i = 60^\circ$ and slightly decreased to 85% at $\theta_i = 80^\circ$, while that of g-C₃N₄-filter sharply decreased to 40% when the incident angle varied from 0° to 80° . In sharp contrast, the photocurrent of the heterostructure decreased by only 20% at $\theta_i = 80^\circ$ as a result of the excellent independence of the optical properties of AZO on the light incident angle. Interestingly enough, the photocurrent of g-C₃N₄/AZO-filter (no UV irradiation) was nearly the same as that g-C₃N₄-filter with perpendicular irradiation due to the unsensitivity of AZO to visible light irradiation

(Fig. S6), while the value only decreased by 19% at $\theta_i = 80^\circ$. The above comprehensive analysis confirmed that the light management properties of the AZO film layer on the heterojunction imparted superior independence of the optical properties from the angle of the incident radiation and endowed the g-C₃N₄/AZO heterojunction photocatalyst with the property of being photosensitized and excited by solar or artificial light at a wide range of incident angles.

Profiting from the uniform distribution of the AZO film, all the AZO-related SEM images showed a worm-like structure (Fig. 2). This morphology was more vermicular after the incubation with *S. marcescens* due to the physical tight attachment of the electrotroph, which could provide better percolation paths and vaster parts of the volume for H⁺, HCO₃⁻ and charge transport in the reduction of inorganic carbon, similar to the favorable morphological worm-like structure of ZnO nanostructures for transparent active layers in solid-state dye-sensitized solar cells [17]. Moreover, the homogeneously distributed EDS mapping of Zn, O, Al, C and N (Fig. S8) indicated the successful synthesis of g-C₃N₄/AZO. Compared to the abiotic electrode, the even distribution of the electrotroph (Fig. 2A, E and I) and the presence of Na, K and P signals in the EDS spectra of the biocathodes (Fig. 2B, F and J) firmly suggested the good biocompatibility of both g-C₃N₄ and AZO. Combining this with the negligible detrimental impact from the flow cytometry measurement (Fig. S9), all the results converged towards the high viability of the g-C₃N₄/AZO photocathode in the photo-assisted MES [30]. In contrast, the redundancy of electrotroph on the g-C₃N₄ cathode (Fig. 2I) severely obstructed the transmission of light to the photocatalyst during the photo-assisted process, thus reducing the solar-to-acetate efficiency.

The XRD pattern (Fig. 3A) and XPS (Fig. 3B) spectra of g-C₃N₄/AZO presented the overlapped characteristic peaks of g-C₃N₄ and AZO, and

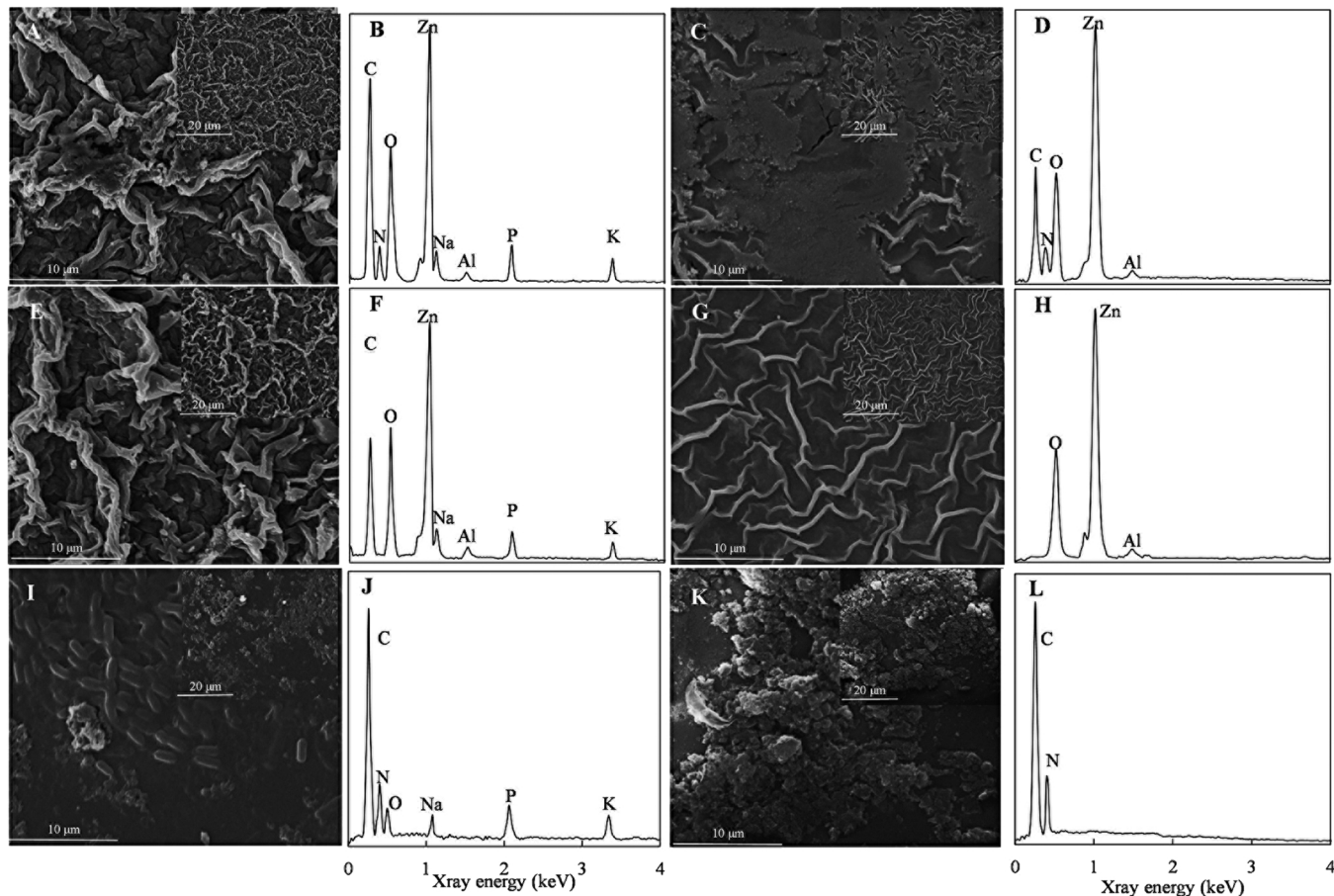


Fig. 2. SEM images on electrodes of g-C₃N₄/AZO (A and C), AZO (E and G), and g-C₃N₄ (I and K) with (A, E and I) or without (C, G and K) *S. marcescens*. EDS spectra of either coverage (B, F and J) or no coverage (D, H, and L) of *S. marcescens* on electrodes of g-C₃N₄/AZO (B and D), AZO (F and H) and g-C₃N₄ (J and L).

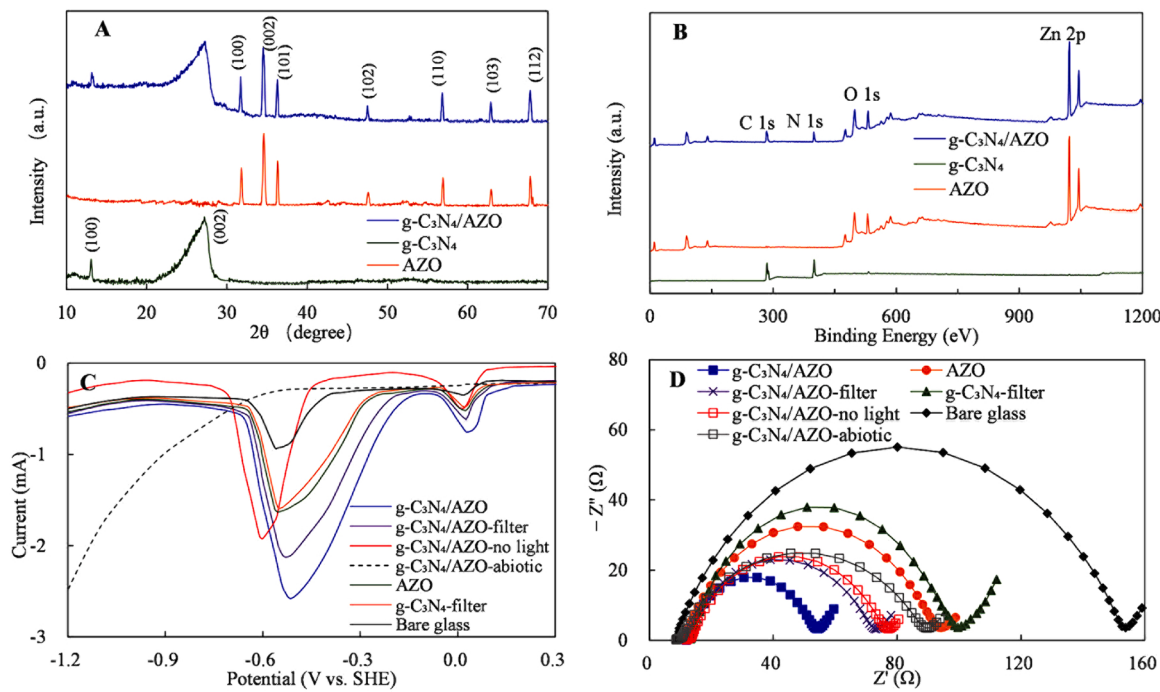


Fig. 3. XRD patterns (A) and XPS survey spectra (B) of various photocatalysts. DPVs (C) and Nyquist plots of EIS (D) of the different *S. marcescens* cathodes and abiotic g-C₃N₄/AZO controls.

firmly proved the successful synthesis of the heterostructure. Particularly, compared to the peak position of AZO or g-C₃N₄, the higher binding energies of Zn 2p and O 1 s or the lower binding energies of C 1 s and N 1 s in g-C₃N₄/AZO XPS results (Fig. S10) confirmed the migration of photogenerated electrons from AZO to g-C₃N₄ following a Z-scheme mechanism in the heterostructure [31], similar to other photocatalytic processes using g-C₃N₄/AZO [26,27].

Discarding the contribution of the heterojunction structure, the DPV plot and EIS spectra (Fig. 3C and D; Table S1; equivalent circuit (Fig. S1)) of g-C₃N₄/AZO-filter exhibited the higher maximum reduction peak current (-2.12 mA) and more positive reduction peak potential (-0.53 V) with lower charge transfer resistance (R_{ct} , 70 Ω) than the g-C₃N₄-filter control (current: -1.58 mA; potential: -0.55 V; R_{ct} : 104 Ω), implying that the light redistribution through the AZO film layer was favorable to the reduction of inorganic carbon in this system. Moreover, the stronger reduction peak around 0.02 V of g-C₃N₄/AZO-filter suggested the participation of a higher fraction of outer membrane c-type cytochromes in the extracellular electron transport [32]. Due to the synergistic effect of the light management layer and the heterojunction structure, the electrochemical analysis of g-C₃N₄/AZO clearly showed the lowest R_{ct} (48 Ω), the strongest reduction peak current (-2.57 mA) and the most positive reduction peak potential (-0.51 V) with the higher amount of c-type cytochromes. The poor performance observed in the control experiment in the absence of light (current: -1.92 mA; potential: -0.60 V; R_{ct} : 76 Ω) demonstrated the significant impact of photo-assistance in such MES and the efficient direct photoinduced electron transfer from the heterojunction to the outer membrane c-type cytochromes enveloping the *S. marcescens* Q1 electrotroph. The decrease of R_{ct} compared to the g-C₃N₄-filter control was not affected by light or dark conditions. This illustrates the favorable impact of the AZO layer to both photocatalysis and electrocatalysis, consistent with other photoelectrocatalysts such as p-ZnTe [33] or NiO/Cu₂O [34] in conventional photoelectrochemical systems. The abiotic controls excluding any false-positive effects by the supporting electrolytes or other electroactive considerations (Fig. 3C and D; Table S1), further reflected the harboring of these electroactive matters for efficient extracellular electron transport.

3.2. Prolonged operation of MES with periodical addition of bicarbonate

A molar ratio of g-C₃N₄ to AZO of 1: 3 (Fig. S11), 6 dip-coating cycles (Fig. S12), a OD₆₀₀ of 0.20 (Fig. S13) and a cathode potential of -1.1 V vs. SHE (Fig. S14) were identified as the optimal operating parameters in this system that yielded the highest acetate production rate and $CE_{acetate}$. Specifically, cathode potentials of -1.1 V ~ -0.6 V vs. SHE led to insignificant differences in acetate production (p : 0.571), $CE_{acetate}$ (p : 0.441) and solar-to-acetate efficiency (p : 0.571), confirming that the light management system was not affected by the cathode potential. Considering that a more negative cathode potential drives a higher electron flux refilling the VB holes of AZO, thus minimizing the recombination of electron–hole pairs of the photocatalyst and improving system performance [35,36], a -1.1 V vs. SHE was chosen as the cathode potential in this study. The gradual consumption of inorganic carbon in the cathodic chamber, resulted in decreased acetate production and $CE_{acetate}$ [37] and in a predicted sharp increased R_{dif} (50 Ω at 1.0 d to 928 Ω at 1.5 d) (Fig. S15, Table S2). Therefore, the continuous efficient production of acetate over 12 days was obtained by a periodical daily addition of bicarbonate.

The g-C₃N₄/AZO photocathode linearly accumulated up to 54.3 ± 0.3 mM (average production rate of 4.5 ± 0.1 mM/d) of acetate over 12 days operation (Fig. 4A), at constant $CE_{acetate}$ of 81 ± 3% (Fig. 4B) and solar-to-acetate efficiency of 1.23 ± 0.05% (Fig. 4C). These results vastly exceeded those obtained with a WO₃/MoO₃/g-C₃N₄ photocathode with the same electrotroph (acetate: 3.1 ± 0.2 mM/d, $CE_{acetate}$: 73 ± 4%, ξ : 0.85 ± 0.09%) [5], and those using a mix-culture CHT/Ni foam biocathode with a BiVO₄/Mo photoanode (acetate: 0.9 ± 0.2 mM/d, $CE_{acetate}$: 62 ± 12%, ξ : 0.97 ± 0.19%) [38].

The significant positive impact of the AZO light management in this system, was independently evaluated by performing experiments with visible light using a 400 nm UV-cut filter to shield the Z-scheme charge transport in the g-C₃N₄/AZO-filter control, since AZO is non-responsive in the visible (Fig. S6). The results obtained with g-C₃N₄/AZO-filter (acetate: 2.4 ± 0.1 mM/d, $CE_{acetate}$: 70 ± 2%, ξ : 0.65 ± 0.03%) were 3.4-fold (acetate, p : 0.017) and 2.3-fold ($CE_{acetate}$, p : 0.024) of those obtained with the g-C₃N₄-filter control (acetate: 0.7 ± 0.2 mM/d,

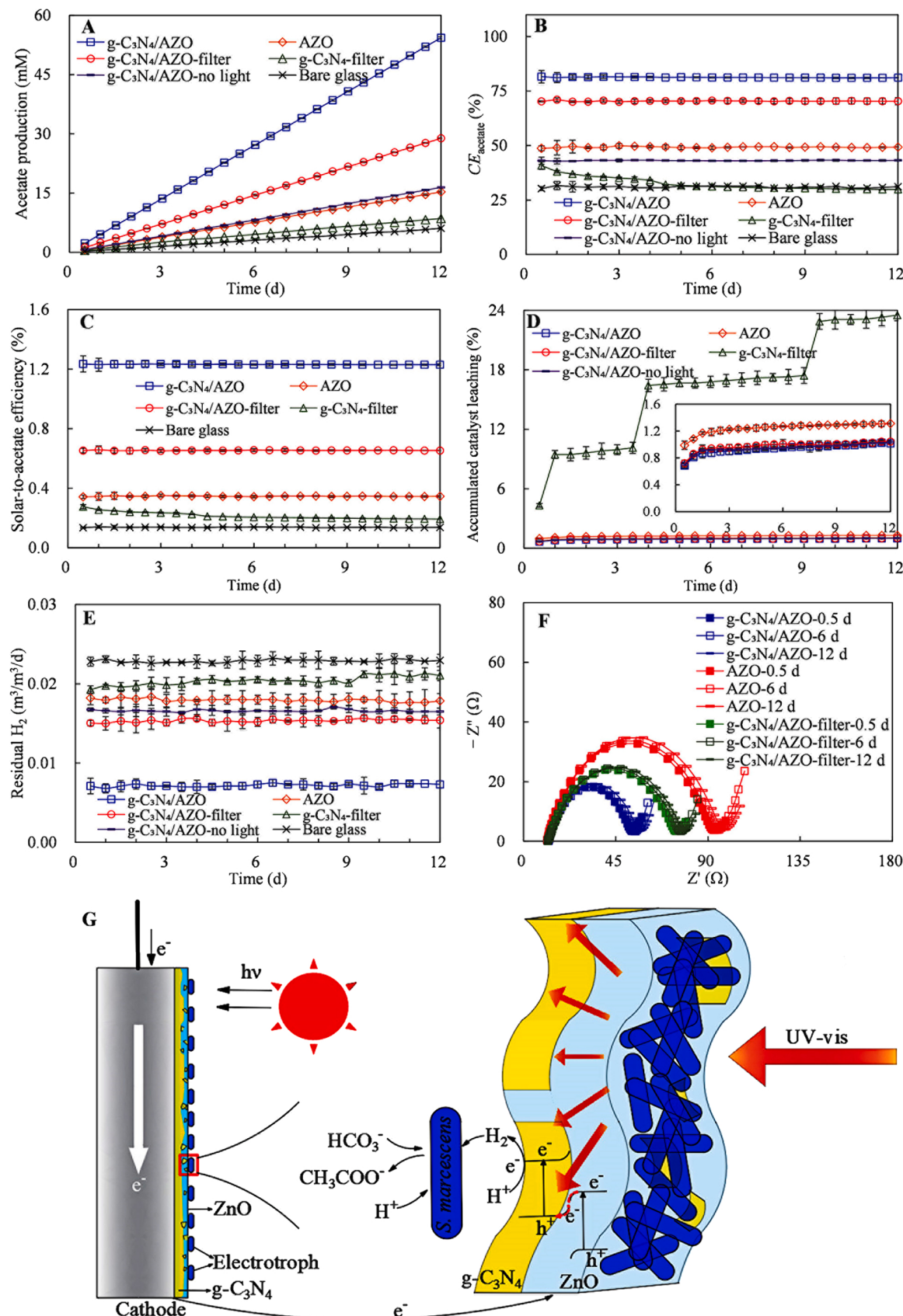


Fig. 4. Acetate production (A), CE_{acetate} (B), solar-to-acetate efficiency (C), accumulated catalyst leaching (D) residual H_2 (E) and Nyquist plots of EIS (F) over a 12-day operation with periodical addition of bicarbonate in the g-C₃N₄/AZO cathodes with or without a 400 nm UV-cut filter under light irradiation or darkness conditions. The photocatalytic mechanism diagram of the light-management AZO film in this photo-assisted MES (G).

CE_{acetate} : $30 \pm 6\%$, ξ : $0.19 \pm 0.05\%$). This 242% (p : 0.016) increase in the solar-to-acetate efficiency based on reducing equivalents as H_2 produced in these experiments, can be attributed to the light management by the AZO film layer. The synergistic interaction of the Z-scheme heterojunction structure and the light management by the AZO film layer resulted in such highly efficient acetate production with 543% (p : 0.003) reducing equivalents increase for the g-C₃N₄/AZO photocathode, compared to the g-C₃N₄-filter control. Moreover, the poor performance observed in the absence of light (acetate: 1.4 ± 0.1 mM/d, CE_{acetate} : $43 \pm 3\%$) reflected the positive and essential role of photo-irradiation and light management in the photo-assisted MES. The small amount of residual hydrogen (Fig. 4E) detected at the headspace of cathode chamber which negatively correlated with acetate production, confirmed the indispensable reducing equivalents (H_2) in the Wood-Ljungdahl pathway for inorganic carbon reduction to acetate [1,4].

Compared to the significantly deteriorated performance observed with the g-C₃N₄-filter control, the acetate production and CE_{acetate} of all AZO-related electrodes remained constant without decay during the 12 days operation. The protection to catalyst leaching offered by the AZO layer, in these prolonged experiments was demonstrated by the insignificant accumulation of catalyst in the cathode solution (Fig. 4D, the AZO-related electrodes: 1%) while significant leaching was observed in its absence (g-C₃N₄-filter control: 24%, p : 0.001). Moreover, the worm-like structure and elementary composition of the g-C₃N₄/AZO bio-photocathode (Fig. S16) observed after 12 days operation was in good agreement with that of the pristine electrode (Fig. 2A). The XRD result of the g-C₃N₄/AZO after DPV (Fig. S17) did not show impurity peaks since it exhibited the same pattern as the fresh electrode, similarly to other studies, where the high chemical stable AZO film was employed as a protective layer to enhance the stability and durability of other photo-electrodes [39–41], further confirming the electrochemical stability of the photocathode. All these converging results, as well as the almost unchanged internal resistance (Fig. 4F and Fig. S16A, Table S3) during the long-term operation of the MES, firmly indicated the excellent chemical stability and robustness of the AZO light-management film layer, which endowed it further broad application prospects in the light management of photo-assisted MES.

3.3. Elucidation of the photocatalytic mechanism

The photocatalytic mechanism over the g-C₃N₄/AZO photocathode illustrated in Fig. 4G shows UV-visible light reaching the surface of the photocatalysts from different incident angles, due to the light rays passing through the electrotropic layer. The incident angle-independent AZO film absorbs a fraction of the UV light producing electron-hole couples, whereas the residual UV and the entire spectrum of visible light trapped in the AZO layer profited from the optimal optical haze of the AZO light management film, ultimately transmitting and scattering photons towards the g-C₃N₄ active layer to generate electron-hole charge pairs. Therefore, a higher fraction of incident photons is utilized by the light management system of the AZO film layer, resulting in a higher number of excited electron-hole pairs in both g-C₃N₄ and AZO. According to the Z-scheme charge transfer mechanism, the photoinduced electrons on the CB of AZO and the photogenerated holes on the VB of g-C₃N₄ recombine at the interface of the heterojunction. Ultimately, the resulting photoinduced electrons on the CB of g-C₃N₄ produce reducing equivalent (H_2), which is consequently metabolized by *S. marcescens* via the Wood-Ljungdahl pathway to trigger inorganic carbon reduction for acetate production [1,4]. The holes left on the VB of AZO are refilled by the electrons arriving from the external circuit drawing a higher current.

This study has forcefully proved the dramatically improved photocatalytic performance of g-C₃N₄ obtained by adding a light-management AZO film, and the efficient performance of the bio-photocatalytic cathode in a MES for the conversion of bicarbonate to acetate. The general applicability of the light-management film layer in photo-assisted MES

was further explored on different photocathodes (MnFe₂O₄/g-C₃N₄ and MnFe₂O₄) developed in our previous study [19]. These were coated with AZO films and experiments using *S. marcescens* Q1 were conducted under illumination with 400 nm UV-cut filters and under the same conditions (Fig. 5). As a result of the improved light management of the AZO film, the MnFe₂O₄/g-C₃N₄/AZO photocathode achieved an outstanding acetate production rate of 11.8 ± 0.5 mM/d and an appreciable ξ of $3.20 \pm 0.12\%$, which was 1.40-fold (acetate, p : 0.031) and 1.38-time (ξ , p : 0.041) higher of that measured with the MnFe₂O₄/g-C₃N₄ control (acetate: 8.5 ± 0.6 mM/d, ξ : $2.32 \pm 0.14\%$). The solar-to-acetate efficiency in this study approaches the reportedly highest value of 3.6% obtained with a Si nanowires/TiO₂/Ni photocathode in photo-assisted MES [3]. However, such study may have exaggerated the role played by the TiO₂ in the Si nanowires/TiO₂/Ni photocathode resulting in an overestimation of the solar-to-acetate efficiency. The light management role of this transparent conductive oxide TiO₂, has been demonstrated in the field of thin-film photovoltaic cells [12,13], but unfortunately being overlooked and only regarded as a

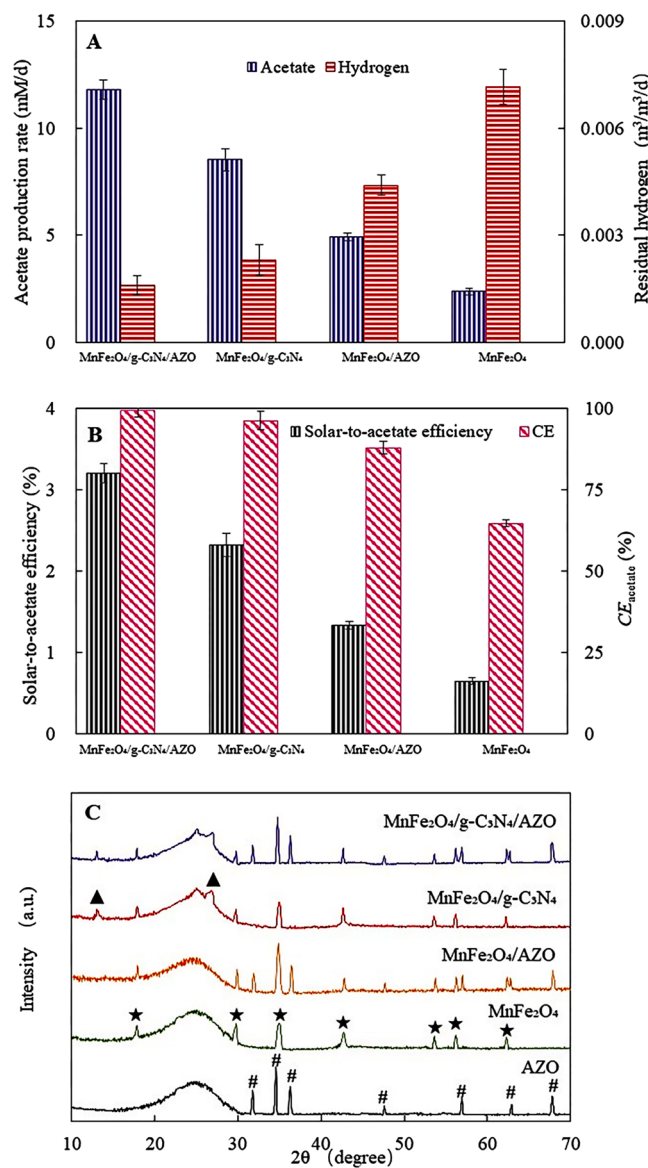


Fig. 5. Acetate production and residual hydrogen (A), CE_{acetate} and solar-to-acetate efficiency (B) of different photocathodes under illumination with 400 nm UV-cut filters. XRD patterns (C) of various photocatalysts with or without the light-management AZO film incorporation.

protective film due to its high resistance to photocorrosion [42] of the Si nanowires/TiO₂/Ni photocathode and thus for stable performance in near-neutral pH electrolyte, as the authors claimed [3]. This incorrect estimation ignoring the light management may have led to an overestimation of the solar-to-acetate efficiency of 3.6%.

Similarly, improved photocatalytic performance was obtained using the MnFe₂O₄/AZO photocathode (acetate: 4.9 ± 0.2 mM/d, ξ : $1.34 \pm 0.05\%$), compared to MnFe₂O₄ control (acetate: 2.4 ± 0.2 mM/d, p : 0.013; ξ : $0.65 \pm 0.04\%$, p : 0.009) due to the enhanced light utilization produced by the light-management AZO film. The higher acetate production corresponding to higher total reducing equivalents H₂ evolution along with lower residual H₂, confirmed again that H₂ acted as a mediator in the inorganic carbon reduction via the Wood-Ljungdahl pathway [1,4,43]. Overall, the dramatically enhanced acetate production in these photo-assisted MES indicated that the light-management film was suitable as an integrated solar management tool for bio-photocathodes, where an efficient photocatalytic performance was achieved even with reduced incident light on the photocatalyst surface.

From a MES development perspective, enhancing the light trapping and harvesting efficiency of the photocathodes with decreased light reflection by employing efficient light management films is not limited to AZO and may be applied to many other transparent conductive oxide thin films such as TiO₂, In₂O₃ and F-doped SnO₂ [12,13]. The scattering, anti-reflection and other photoelectric properties of these films can function as a light manager to improve the light utilization within the photoactive layer of the cathodes, enabling augmented reducing equivalents generation and thus efficient value-added outputs in the photo-assisted MES. Considering the good biocompatibility of the selected transparent conductive oxides, these light management films can also be applied to other model electrotrophs (such as *M. thermoacetica* and *S. ovata*), which frequently serve as biocatalysts in many other photo-assisted MESs. Theoretically, the light management is fully related with the physical interface between semiconductors and the electrotrophs regardless of the electrotrrophic inherent characters and microbial physiology. The light management system is not correlated with a particular reactor configuration but depends on the efficacy of light irradiation of the photoelectrode, similar to sunlight absorption by photovoltaic technologies [44] or the solar absorber material in photothermal water vaporization system [45]. Collectively, the optical and physical aspects of the light management system guarantee its universal application to any other electrotrroph coupled with any other transparent conductive oxides and in any other reactor architecture.

The most impactful studies moving forward should establish the quantitative correlation between light management and the electrotrrophic coverage of the cathode including the interior fibrous structure of the graphite felt support, and should develop a standardized set of guidelines to achieve efficient light management in photo-assisted MES.

4. Conclusions

This study has for the first time combined a light-management film layer with a bio-photocathode to enhance significantly the production of acetate in photo-assisted MES. Taking AZO film as an example and the g-C₃N₄ as an active photocatalytic layer, the shielding of the incident light caused by the electrotrophs on the bio-photocathodes was overcome as a result of the optical properties of the AZO film layer which redistributed the incident light over the photoactive later. Enhanced light trapping and reduced light reflection within the active layer resulted from the high transparency and tuned optical haze of the AZO film, achieved more reducing equivalents production as H₂ to 242% (g-C₃N₄/AZO-filter) and 543% (g-C₃N₄/AZO) with increased CE_{acetate} of 70% (g-C₃N₄/AZO-filter) and 81% (g-C₃N₄/AZO). The general applicability of the light-management film to other semiconductive bio-cathodes (MnFe₂O₄ and MnFe₂O₄/g-C₃N₄) and significantly enhanced photocatalytic performance was demonstrated after incorporation of a AZO light management film with a record high solar-to-acetate efficiency of 3.20% for

the MnFe₂O₄/g-C₃N₄/AZO biocathode. Along with any other model or non-model electrotrophs, as well as other carbon-prolonged products such as medium-chain carboxylates and even bioplastics through inorganic carbon conversion in microbial photoelectrochemical systems coupled with microbial fermentation processes, the light management system described here might also expand in other exciting and promising areas. This study opens up a new opportunity to construct efficient bio-photocathodes through effective use of a light management system, and thus allows the tailoring and manipulation of photo-assisted MES towards the desired synthesis products from CO₂ sequestration.

Ethical statement

Compliance with Ethical Standards.

CRediT authorship contribution statement

Weifeng Kong: Conceptualization, Methodology, Data curation, Writing – original draft. **Liping Huang:** Conceptualization, Investigation, Supervision, Validation, Writing – review & editing. **Xie Quan:** Supervision, Writing – review & editing. **Gianluca Li Puma:** Visualization, Writing – review & editing.

Declaration of Competing Interest

The authors declare that they have no known competing financial interests or personal relationships that could have appeared to influence the work reported in this paper.

Data Availability

Data will be made available on request.

Acknowledgements

The authors gratefully acknowledge financial support from the National Natural Science Foundation of China (Nos. 22276025 and 52070032) and the Fundamental Research Funds for the Central Universities (No. DUT21LAB101).

Appendix A. Supporting information

Supplementary data associated with this article can be found in the online version at doi:10.1016/j.apcatb.2022.122247.

References

- [1] K.K. Sakimoto, S.J. Zhang, P.D. Yang, Cysteine-cystine photoregeneration for oxygenic photosynthesis of acetic acid from CO₂ by a tandem inorganic-biological hybrid system, Nano Lett. 16 (2016) 5883–5887, <https://doi.org/10.1021/acs.nanolett.6b02740>.
- [2] E. Blanchet, F. Duquenne, Y. Rafrafi, L. Etcheverry, B. Erable, A. Bergel, Importance of the hydrogen route in up-scaling electrosynthesis for microbial CO₂ reduction, Energy Environ. Sci. 8 (2015) 3731–3744, <https://doi.org/10.1039/c5ee03088a>.
- [3] Y.D. Su, S. Cestellos-Blanco, J.M. Kim, Y.X. Shen, Q. Kong, D.L. Lu, C. Liu, H. Zhang, Y.H. Cao, P.D. Yang, Close-packed nanowire-bacteria hybrids for efficient solar-driven CO₂ fixation, Joule 4 (2020) 800–811, <https://doi.org/10.1016/j.joule.2020.03.001>.
- [4] N.S. Welivatte, S.D. Minteer, Photo-bioelectrocatalytic CO₂ reduction for a circular energy landscape, Joule 5 (2021) 2564–2592, <https://doi.org/10.1016/j.joule.2021.08.003>.
- [5] Z.H. Cai, L.P. Huang, X. Quan, Z.B. Zhao, Y. Shi, G. Li-Puma, Acetate production from inorganic carbon (HCO₃⁻) in photo-assisted biocathode microbial electrosynthesis systems using WO₃/MoO₃/g-C₃N₄ heterojunctions and *Serratia marcescens* species, Appl. Catal. B Environ. 267 (2020), 118611, <https://doi.org/10.1016/j.apcatb.2020.118611>.
- [6] K. Kuruvinashetti, N. Kornienko, Pushing the methodological envelope in understanding the photo/electrosynthetic materials-microorganism interface, iScience 24 (2021), 103049, <https://doi.org/10.1016/j.isci.2021.103049>.

- [7] Y. Yao, J. Yao, V.K. Narasimhan, Z.C. Ruan, C. Xie, S.H. Fan, Y. Cui, Broadband light management using low-Q whispering gallery modes in spherical nanoshells, *Nat. Commun.* 3 (2012) 664, <https://doi.org/10.1038/ncomms1664>.
- [8] C. Chen, S.J. Zheng, H.W. Song, Photon management to reduce energy loss in perovskite solar cells, *Chem. Soc. Rev.* 50 (2021) 7250–7329, <https://doi.org/10.1039/d0cs01488e>.
- [9] Y.G. Wang, T. Li, Y.G. Yao, X. Li, X. Bai, C.C. Yin, N. Williams, S.F. Kang, L.F. Cui, L. B. Hu, Dramatic enhancement of CO₂ photoreduction by biodegradable light-management paper, *Adv. Energy Mater.* 8 (2018) 1703136, <https://doi.org/10.1002/aenm.201703136>.
- [10] J.Y.Y. Loh, A. Mohan, A.G. Flood, G.A. Ozin, N.P. Kherani, Waveguide photoreactor enhances solar fuels photon utilization towards maximal optoelectronic–photocatalytic synergy, *Nat. Commun.* 12 (2021) 402, <https://doi.org/10.1038/s41467-020-20613-2>.
- [11] S. Xiao, Q. Fu, Z. Li, J. Li, L. Zhang, X. Zhu, Q. Liao, Solar-driven biological inorganic hybrid systems for the production of solar fuels and chemicals from carbon dioxide, *Renew. Sustain. Energy Rev.* 150 (2021), 111375, <https://doi.org/10.1016/j.rser.2021.111375>.
- [12] K. Ellmer, Past achievements and future challenges in the development of optically transparent electrodes, *Nat. Photon* 6 (2012) 808–816, <https://doi.org/10.1038/nphoton.2012.282>.
- [13] C. Wu, K. Wang, M. Batmunkh, A.S.R. Bati, D. Yang, Y.Y. Jiang, Y.C. Hou, J. G. Shapter, S. Priya, Multifunctional nanostructured materials for next generation photovoltaics, *Nano Energy* 70 (2020), 104480, <https://doi.org/10.1016/j.nano.2020.104480>.
- [14] X.B. Chen, G.Y. Xu, G. Zeng, H.W. Gu, H.Y. Chen, H.T. Xu, H.F. Yao, Y.W. Li, J. H. Hou, Y.F. Li, Realizing ultrahigh mechanical flexibility and >15% efficiency of flexible organic solar cells via a “welding” flexible transparent electrode, *Adv. Mater.* 32 (2020) 1908478, <https://doi.org/10.1002/adma.201908478>.
- [15] J.W. Fu, J.G. Yu, C.J. Jiang, B. Cheng, g-C₃N₄-Based heterostructured photocatalysts, *Adv. Energy Mater.* 8 (2018) 1701503, <https://doi.org/10.1002/aenm.201701503>.
- [16] W.F. Kong, L.P. Huang, X. Quan, Z.B. Zhao, G. Li-Puma, Efficient production of acetate from inorganic carbon (HCO₃⁻) in microbial electrosynthesis systems incorporating Ag₃PO₄/g-C₃N₄ anaerobic photo-assisted biocathodes, *Appl. Catal. B-Environ.* 284 (2021), 119696, <https://doi.org/10.1016/j.apcatb.2020.119696>.
- [17] K. Wang, V. Korstgens, D. Yang, N. Hohn, S.V. Roth, P. Muller-Buschbaum, Morphology control of low temperature fabricated ZnO nanostructures for transparent active layers in all solid-state dye-sensitized solar cells, *J. Mater. Chem. A* 6 (2018) 4405–4415, <https://doi.org/10.1039/c7ta10654h>.
- [18] Z.N. Ng, K.Y. Chan, T. Tohsophon, Effects of annealing temperature on ZnO and AZO films prepared by sol–gel technique, *Appl. Surf. Sci.* 258 (2012) 9604–9609, <https://doi.org/10.1016/j.apsusc.2012.05.156>.
- [19] W.F. Kong, L.P. Huang, X. Quan, G. Li-Puma, Synergistic induced charge transfer switch by oxygen vacancy and pyrrolic nitrogen in MnFe₂O₄/g-C₃N₄ heterojunctions for efficient transformation of bicarbonate to acetate in photo-assisted MES, *Appl. Catal. B-Environ.* 307 (2022), 121214, <https://doi.org/10.1016/j.apcatb.2022.121214>.
- [20] A. Ter Heijne, O. Schaezel, S. Gimenez, F. Fabregat-Santiago, J. Bisquert, D.P.B.T. B. Strik, F. Barriere, C.J.N. Buisman, H.V.M. Hamelers, Identifying charge and mass transfer resistances of an oxygen reducing biocathode, *Energy Environ. Sci.* 4 (2011) 5035, <https://doi.org/10.1039/C1EE02131A>.
- [21] X. Dominguez-Benetton, S. Sevda, K. Vanbroekhoven, D. Pant, The accurate use of impedance analysis for the study of microbial electrochemical systems, *Chem. Soc. Rev.* 41 (2012) 7228–7246, <https://doi.org/10.1039/c2cs35026b>.
- [22] R. Ranjan, M. Kumar, A.S.K. Sinha, CdS supported on electrochemically reduced rGO for photo reduction of water to hydrogen, *Int. J. Hydron. Energ.* 44 (2012) 10573–10584, <https://doi.org/10.1016/j.ijhydene.2019.02.195>.
- [23] Q. Wang, L.P. Huang, X. Quan, G. Li-Puma, Sequential anaerobic and electro-Fenton processes mediated by W and Mo oxides for degradation/mineralization of azo dye methyl orange in photo assisted microbial cells, *Appl. Catal. B-Environ.* 245 (2019) 672–680, <https://doi.org/10.1016/j.apcatb.2019.01.026>.
- [24] G. Kang, K. Bae, M. Nam, D.H. Ko, K. Kim, W.J. Padilla, Broadband and ultrahigh optical haze thin films with self-aggregated alumina nanowire bundles for photovoltaic applications, *Energy Environ. Sci.* 8 (2015) 2650–2656, <https://doi.org/10.1039/c5ee01757b>.
- [25] D.T. Liu, J. Whitehead, M.R. Alfara, E. Reyes-Villegas, D.V. Spracklen, C. L. Reddington, S.F. Kong, P.I. Williams, Y.C. Ting, S. Haslett, J.W. Taylor, M. J. Flynn, W.T. Morgan, G. McFiggans, H. Coe, J.D. Allan, Black-carbon absorption enhancement in the atmosphere determined by particle mixing state, *Nat. Geosci.* 10 (2017) 184–188, <https://doi.org/10.1038/ngeo2901>.
- [26] S.K. Le, T.S. Jiang, Y.W. Li, Q. Zhao, Y.Y. Li, W.B. Fang, M. Gong, Highly efficient visible-light-driven mesoporous graphitic carbon nitride/ZnO nanocomposite photocatalysts, *Appl. Catal. B-Environ.* 200 (2017) 601–610, <https://doi.org/10.1016/j.apcatb.2016.07.027>.
- [27] D. Kim, K. Yong, Boron doping induced charge transfer switching of a C₃N₄/ZnO photocatalyst from Z-scheme to type II to enhance photocatalytic hydrogen production, *Appl. Catal. B Environ.* 282 (2017), 119538, <https://doi.org/10.1016/j.apcatb.2020.119538>.
- [28] F.K. Meng, J.T. Li, S.K. Cushing, M.J. Zhi, N.Q. Wu, Solar hydrogen generation by nanoscale p-n junction of p-type molybdenum disulfide/n-type nitrogen-doped reduced graphene oxide, *J. Am. Chem. Soc.* 135 (2013) 10286–10289, <https://doi.org/10.1021/ja404851s>.
- [29] S.Q. Wu, X.J. Tan, J.Y. Lei, H.J. Chen, L.Z. Wang, J.L. Zhang, Ga-doped and Pt-loaded porous TiO₂/SiO₂ for photocatalytic nonoxidative coupling of methane, *J. Am. Chem. Soc.* 141 (2019) 6592–6600, <https://doi.org/10.1021/jacs.8b13858>.
- [30] J. Ye, J. Yu, Y.Y. Zhang, M. Chen, X. Liu, S.G. Zhou, Z. He, Light-driven carbon dioxide reduction to methane by *Methanoscincus barkeri*-CdS biohybrid, *Appl. Catal. B-Environ.* 257 (2019), 117916, <https://doi.org/10.1016/j.apcatb.2019.117916>.
- [31] W.X. Chang, W.H. Xue, E.Z. Liu, J. Fan, B.R. Zhao, Highly efficient H₂ production over NiCo₂O₄ decorated g-C₃N₄ by photocatalytic water reduction, *Chem. Eng. J.* 362 (2019) 392–401, <https://doi.org/10.1016/j.cej.2019.01.021>.
- [32] Y. Xiao, E.H. Zhang, J.D. Zhang, Y.F. Dai, Z.H. Yang, H.E.M. Christensen, J. Ulstrup, F. Zhao, Extracellular polymeric substances are transient media for microbial extracellular electron transfer, *Sci. Adv.* 3 (2017), e1700623, <https://doi.org/10.1126/sciadv.1700623>.
- [33] D.H. Won, J. Chung, S.H. Park, E.H. Kim, S.I. Woo, Photoelectrochemical production of useful fuels from carbon dioxide on a polypyrrole-coated p-ZnTe photocathode under visible light irradiation, *J. Mater. Chem. A* 3 (2015) 1089–1095, <https://doi.org/10.1039/c4ta05901h>.
- [34] C.K. Mavrokefalos, M. Hasan, J.F. Rohan, R.G. Compton, J.S. Foord, Electrochemically deposited Cu₂O cubic particles on boron doped diamond substrate as efficient photocathode for solar hydrogen generation, *Appl. Surf. Sci.* 408 (2017) 125–134, <https://doi.org/10.1016/j.apsusc.2017.02.148>.
- [35] Y.B. Ding, C.Z. Yang, L.H. Zhu, J.D. Zhang, Photoelectrochemical activity of liquid phase deposited TiO₂ film for degradation of benzotriazole, *J. Hazard. Mater.* 175 (2010) 96–103, <https://doi.org/10.1016/j.jhazmat.2009.09.037>.
- [36] Y.P. Hou, Y.Y. Gan, Z.B. Yu, X.X. Chen, L. Qian, B.G. Zhang, L.R. Huang, J. Huang, Solar promoted azo dye degradation and energy production in the bio-photoelectrochemical system with a g-C₃N₄/BiOBr heterojunction photocathode, *J. Power Sources* 371 (2017) 26–34, <https://doi.org/10.1016/j.jpowsour.2017.10.033>.
- [37] G. Mohanakrishna, K. Vanbroekhoven, D. Pant, Impact of dissolved carbon dioxide concentration on the process parameters during its conversion to acetate through microbial electrosynthesis, *React. Chem. Eng.* 3 (2018) 371–378, <https://doi.org/10.1039/C7RE00220C>.
- [38] B. Bian, L. Shi, K.P. Katuri, J.J. Xu, P. Wang, P.E. Saikaly, Efficient solar-to-acetate conversion from CO₂ through microbial electrosynthesis coupled with stable photoanode, *Appl. Energ.* 278 (2020), 115684, <https://doi.org/10.1016/j.apenergy.2020.115684>.
- [39] A. Paracchino, V. Laporte, K. Sivula, M. Grätzel, E. Thimsen, Highly active oxide photocathode for photoelectrochemical water reduction, *Nat. Mater.* 10 (2011) 456–461, <https://doi.org/10.1038/nmat3017>.
- [40] A. Paracchino, N. Mathews, T. Hisatomi, M. Stefk, S.D. Tilley, M. Grätzel, Ultrathin films on copper (I) oxide water splitting photocathodes: a study on performance and stability, *Energy Environ. Sci.* 5 (2012) 8673–8781, <https://doi.org/10.1039/c2ee22063f>.
- [41] W. Yang, R.R. Prabhakar, J. Tan, S.D. Tilley, J. Moon, Strategies for enhancing the photocurrent, photovoltage, and stability of photoelectrodes for photoelectrochemical water splitting, *Chem. Soc. Rev.* 48 (2019) 4979–5015, <https://doi.org/10.1039/c8cs00997j>.
- [42] Y.J. Hwang, A. Boukal, P.D. Yang, High density n-Si/n-TiO₂ core/shell nanowire arrays with enhanced photoactivity, *Nano Lett.* 9 (2009) 410–415, <https://doi.org/10.1021/nl8032763>.
- [43] D.A. Moreno-Jimenez, K.Y. Kim, Enhanced wettability improves catalytic activity of nickel-functionalized activated carbon cathode for hydrogen production in microbial electrolysis cells, *Bioresour. Technol.* 350 (2022), 126881, <https://doi.org/10.1016/j.biortech.2022.126881>.
- [44] M.M. Fouad, L.A. Shihata, E.I. Morgan, An integrated review of factors influencing the performance of photovoltaic panels, *Renew. Sustain. Energ. Rev.* 80 (2017) 1499–1511, <https://doi.org/10.1016/j.rser.2017.05.141>.
- [45] M.M. Gao, L.L. Zhu, C.K. Peh, G.W. Ho, Solar absorber material and system designs for photothermal water vaporization towards clean water and energy production, *Energy Environ. Sci.* 12 (2019) 841–864, <https://doi.org/10.1039/c8ee01146j>.